Modeling and validation of single-chamber microbial fuel cell cathode biofilm growth and response to oxidant gas composition

Shiqi Ou^{a,b}, Yi Zhao^c, Douglas S. Aaron^a, John M. Regan^c, Matthew M. Mench^{a,*}

^aDepartment of Mechanical, Aerospace and Biomedical Engineering, the University of Tennessee, Knoxville TN, 37996, USA;

^bOak Ridge National Laboratory, Knoxville TN, 37932, USA;

^cDepartment of Civil & Environmental Engineering, the Pennsylvania State University, University Park PA, 16801, USA.

Citation: Ou, S., Zhao, Y., Aaron, D.S., Regan, J.M. and Mench, M.M., 2016. Modeling and validation of single-chamber microbial fuel cell cathode biofilm growth and response to oxidant gas composition. Journal of Power Sources, 328, pp.385-396.

doi: https://doi.org/10.1016/j.jpowsour.2016.08.007.

This manuscript has been authored by UT-Battelle, LLC under Contract No. DE-AC05-00OR22725 with the U.S. Department of Energy. The United States Government retains and the publisher, by accepting the article for publication, acknowledges that the United States Government retains a nonexclusive, paid-up, irrevocable, world-wide license to publish or reproduce the published form of this manuscript, or allow others to do so, for United States Government purposes. The Department of Energy will provide public access to these results of federally sponsored research in accordance with the DOE Public Access Plan (http://energy.gov/downloads/doe-public-access-plan)

Abstract

This work describes experiments and computational simulations to analyze single chamber, air cathode microbial fuel cell (MFC) performance and cathodic limitations in terms of current generation, power output, mass transport, biomass competition, and biofilm growth. Steady-state and transient cathode models were developed and experimentally validated. Two cathode gas mixtures were used to explore oxygen transport in the cathode: the MFCs exposed to a helium-oxygen mixture (heliox) produced higher current and power output than the group of MFCs exposed to air or a nitrogen-oxygen mixture (nitrox), indicating a dependence on gas-phase transport in the cathode. Multi-substance transport, biological reactions, and electrochemical reactions in a multi-layer and multi-biomass cathode biofilm were also simulated in a transient model. The transient model described biofilm growth over 15 days while providing insight into mass transport and cathodic dissolved species concentration profiles during biofilm growth. Simulation results predict that the dissolved oxygen content and diffusion in the cathode are key parameters affecting the power output of the air-cathode MFC system, with greater oxygen content in the cathode resulting in increased power output and fully-matured biomass.

Keywords:

Microbial fuel cell; computational simulation; oxygen transport; cathodic biofilm growth; transient model.

Final Manuscript Version

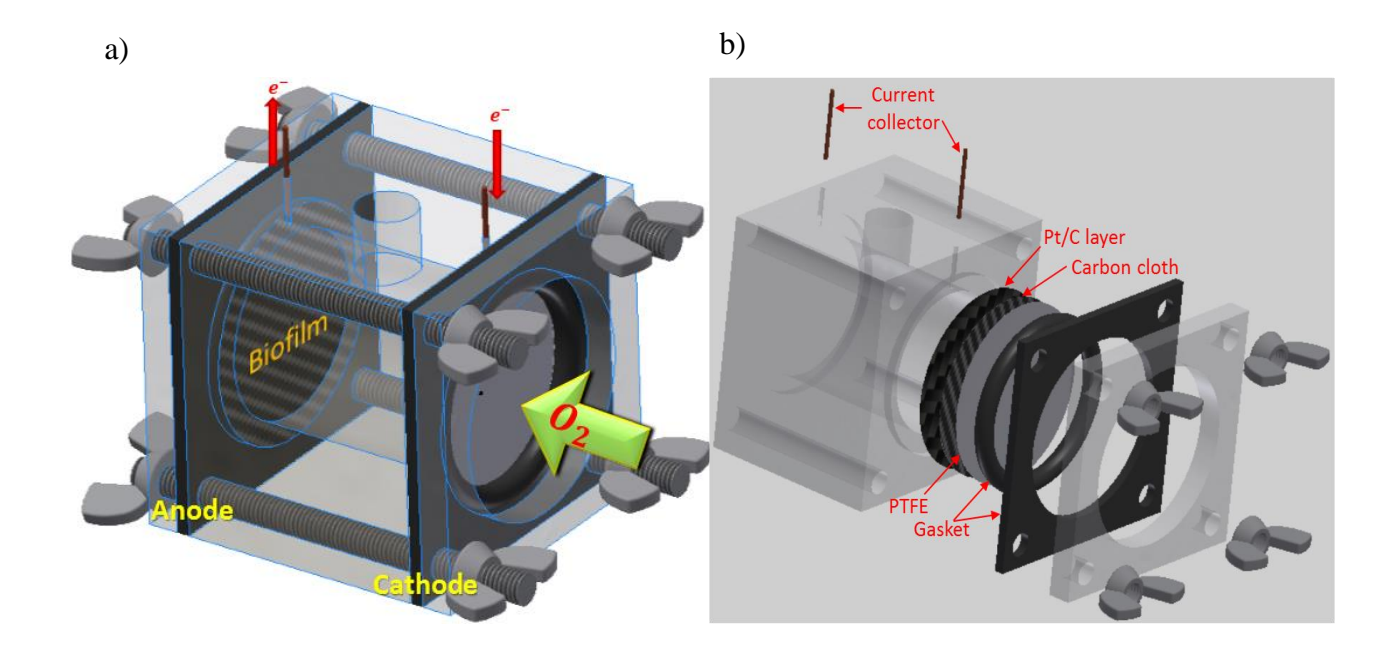
* Corresponding author at: Electrochemical Energy Storage and Conversion Laboratory,
Department of Mechanical, Aerospace, and Biomedical Engineering, The University of
Tennessee, Knoxville, TN 37996, USA. Tel.: +1 (865)974 6751.

E-mail address: mmench@utk.edu (M.M. Mench).

1. Introduction

Sustainable energy for future energy security intersects with wastewater treatment in microbial fuel cells (MFCs). MFCs incorporate electrochemical and biological reactions to produce electricity during the treatment of wastewater, traditionally an energy-consuming process. This operation is enabled by exoelectrogens, biomass able to transport electrons outside their cell walls [1]. Despite the conceptual promise of MFCs, low relative power output per active area [2] and use of expensive catalysts on the cathode continue to prevent them from being economically competitive with traditional treatment strategies. Thus, current efforts typically focus on improving the power density of MFCs or identifying better materials to reduce system costs. Fig. 1 a) illustrates the single chamber air-cathode MFC reactor that improves system economy by excluding an expensive polymer electrolyte to separate the anode and cathode. In addition to lower cost, the single chamber MFC benefits from reduced internal resistance [3], enabling improved performance. On the anode side, the exoelectrogenic biomass form a biofilm directly on the electrode material, providing electrical contact with the external circuit. The cathode is exposed to the atmosphere, allowing an oxygen supply for the oxygen reduction reaction (ORR) which consumes electrons generated in the anode.

Recent research efforts have identified the cathode as the limiting component of certain MFC designs, affecting biomass growth and electrochemical reactions throughout the reactor [3-7]. Performance loss in these can be separated into three types of overpotential: kinetic activation loss, ohmic loss, and mass transport loss [3]. Oxygen transport limitations have become increasingly prominent with continued advances in MFC performance and are thus of greater interest [8]. The results of Santoro et al.'s experiments showed that cathodic structure affects performance and power output in MFC reactor [7]. The cathode structure that incorporated a



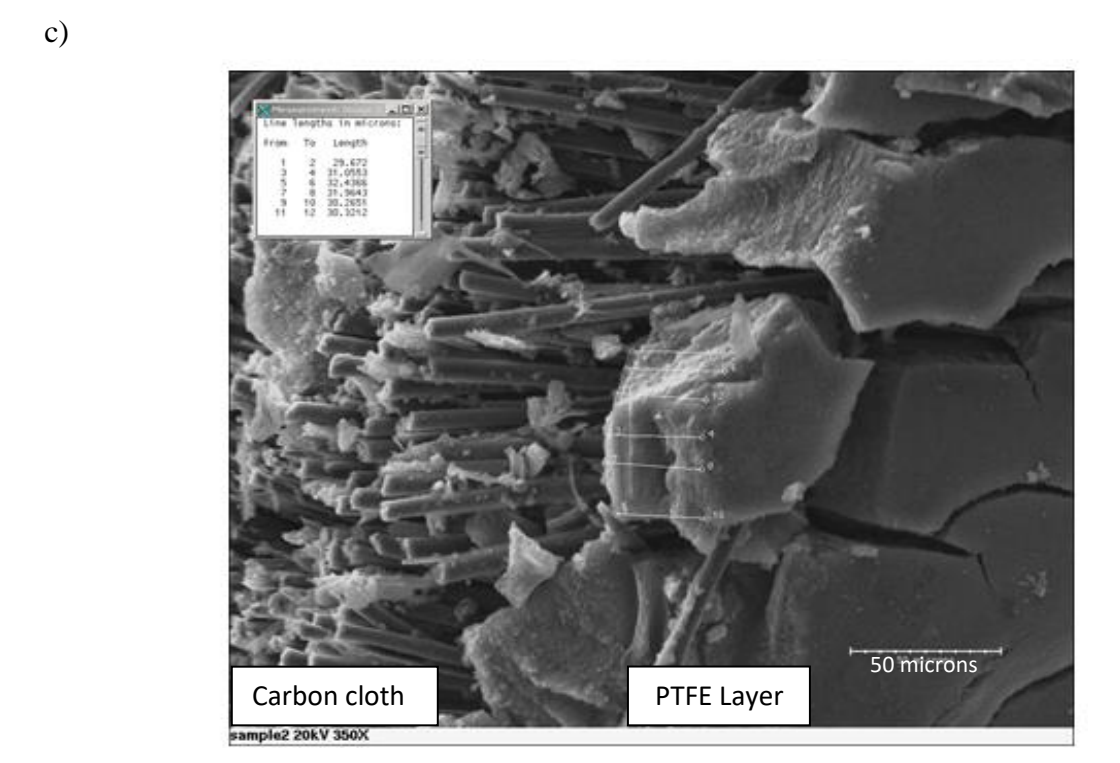


Figure 1. a) Schematic of single chamber air-cathode MFC reactor; b) Exploded schematic of the cathode-side structure; c) Scanning electron microscope (SEM) picture for MFC cathodic materials.

microporous layer inserted between the catalyst layer and the diffusion layer exhibited low water loss, high power generation and efficient contaminant removal [7]. Additionally, experiments have shown that the cathodic biofilm can accept electrons directly from the cathode, which positively affects the MFC cathode [9]. In addition to participating in the passage of electrical current, the cathode biofilm also consumes oxygen before it can reach the anode. Previous steady state cathode simulations predict that the biocatalyst contributes approximately 9 % of cell power production while the metal catalyst contributes approximately 91 % of the power in the single chamber aircathode MFC reactor [10, 11].

Computational simulations of electrochemical reactions and biomass growth processes have offered insight into the limiting processes that occur in MFCs. The first component of this work was the development of a steady state model for the cathode in an air-cathode MFC reactor, specifically to simulate the cathodic mass transport, power generation, and polarization curves with varying external resistors. Experimental work indicated that the amount and flux of oxygen in the cathode strongly affects MFC performance, thus the experimental and simulation results were compared to explore the oxygen transport mechanism in the cathode. In the steady state model, the distribution and the amount of gaseous oxygen, dissolved oxygen and the associated current densities are calculated; additionally, the concentrations of other species (nitrogen, helium, oxygen, acetate, hydroxide etc.) in the cathode are considered. A one-dimensional transient model for the single chamber MFC was also developed; this model focused on the dynamic changes for mixed cultures of attached and suspended biomass, cathodic biofilm, and mass transport in both the cathode and bulk liquid. Because the cathode can be considered a transition region from an aerobic to an anaerobic environment, the microbial composition of the cathode biofilm is complex and contains at least three components: active biomass of a mixture of cultures, inert biomass, and

extracellular polymeric substance (EPS) which significantly influences biofilm electron conductivity. The EPS of the biofilm matrix encases the biofilm cells, anchors them to the electrode, and also houses electroactive components of the biofilm matrix [12]. This work considers the competition that occurs in the cathode biofilm during the transient growth phase and the influence of mass transport on other processes in the reactor.

2. Model Formulation

The goal of this modeling effort and related experiments is to describe and analyze the relationship among several factors, to identify the dominant factors which influence COD degradation and power output, and to gain insight that can lead to an improved design of the MFC. This model was focused on both steady-state and transient cathode behavior, specifically mass transport and its effects on MFC performance and microbial growth.

2.1. Cathode Structure and Domains

The MFC physical structure had dimensions of 4 cm diameter × 4 cm length from the air interface on the cathode to the current collector on the anode; Fig. 1 a) is the single chamber cube reactor, and Fig. 1 b) shows the cathode structure. The MFC cathode properties have significant effects on power generation, thus the materials and structure are of great interest [7]. In this study, the MFC reactor is composed of several layers, described from the air side to the anaerobic anode: a hydrophobic PTFE layer for water management, hydrophilic carbon cloth that is saturated with growth medium, and the Pt/C catalyst layer where the ORR occurs. The PTFE layer is relatively dense and hydrophobic, which does not allow significant liquid water accumulation under normal operating conditions. The carbon cloth layer is irregularly composed of porous, reticulated carbon fibers, enabling diffusion of dissolved species and conduction of electrons. The Pt/C catalyst layer

is comprised of agglomerates of catalyst nanoparticles anchored on carbon microparticles with high tortuosity and porosity. The cathode biofilm is assumed to be uniformly attached to the catalyst layer. A representative scanning electron micrograph of the layered cathode is shown in Fig. 1 c).

Based on the physical structure of the cathode materials, the cathodic modeling domains were divided into 6 regions: the PTFE layer, the carbon cloth, the Pt/C catalyst layer, the cathodic biofilm, a diffusion boundary layer bordering the bulk liquid, and the bulk liquid. The carbon cloth and Pt/C catalyst layers are both saturated with liquid in normal operating conditions. The cathode biofilm competes with the microbial anode for the carbon source, resulting in a negative impact on MFC performance; however, the cathode biofilm also consumes oxygen, minimizing the infiltration and crossover of oxygen to the anode, resulting in a net positive effect on cell performance. The cathode biofilm is actually composed of two broad populations – autotrophic aerobic biomass (AAB) and heterotrophic aerobic biomass (HAB). The AAB receives electrons directly from the electrode while consuming oxygen; the HAB consumes the carbon source (such as acetate) in competition with the anode while also consuming oxygen.

2.2. Experiments

Experiments were conducted on cubic MFCs [2] with a gas sparging chamber (14 mL volume). The anode material was a graphite fiber brush, 25 mm long and 25mm diameter. The fiber type was PANEX (33 160 K, ZOLTEK). The anode brush was heat treated at 450 °C for 30 min [13, 14]. The cathodes consisted of four layers of PTFE, whose preparation is described elsewhere [5]. All reactors were inoculated with a stable power production MFC culture and were fed a growth medium described in Ren et. al. [15]. In order to study the effect of oxygen transport on power

generation of MFCs, the performance of heliox- (21 % oxygen, 79 % helium), nitrox- (21 % oxygen, 79 % nitrogen), and laboratory air-supplied reactors were compared. During the experiments, the gas flow rate past the cathode was reduced from 5 L/h to 2 L/h to study mass transport limitations [16]. Polarization and power density results were obtained by using different external resistances at 20-minute intervals with voltage (V_{cell}) measured by a Keithley 2700 Digital Multimeter. Electrochemical impedance spectroscopy (EIS) and linear sweep voltammetry (LSV) were performed with a potentiostat (BioLogic VMP3) and compared to a Ag/AgCl reference electrode (BASi).

2.3. Model assumptions

Steady state model: In an effort to focus on changes in the cathode, this simulation utilized fixed bulk liquid acetate concentration (c_{Ac} = 800 mg/L) and pH (pH = 7.08). The bulk liquid, in practice, includes a buffer to maintain the bulk liquid pH, supporting this assumption. In addition to an unchanging bulk liquid environment, the cathode biofilm was assumed to be fully grown, meaning that the biofilm thickness and biomass concentration were constant. Additionally, the biofilm detachment rate and attachment rate were balanced. Because polarization curves with an experimental MFC were conducted with external resistors, the model simulated the electrochemical parameters using external resistance as the control variable. Oxygen diffusing into the PTFE layer was considered in the gas-phase only since liquid water is excluded from this region due to high hydrophobicity. Upon crossing the boundary between the PTFE layer and the carbon cloth, oxygen dissolved in the liquid in the carbon cloth according to Henry's law. In the experimental work, a significant difference in MFC performance was observed when heliumoxygen and nitrogen-oxygen (heliox and nitrox, respectively) gas mixtures were used at the cathode instead of air [16]. Since dissolved oxygen depends only on the gas-phase partial pressure

of oxygen, this difference in performance indicated that gas was present in the carbon cloth and catalyst layers; this behavior is considered here.

Transient state model: Cathode biofilm growth, competition between two biomass metabolic cultures, and the mass transport changes in both bulk liquid and cathode over 15 days are described in the transient model. The domains, primary boundary conditions, and the initial values in this model are shown in Fig. 2 a). The initial growth medium conditions were similar to the steady state model in which the acetate concentration was 800 mg/L and the pH was 7.08. The cathode (except the PTFE layer) was initially assumed to be fully saturated, allowing oxygen to dissolve into and through the liquid. The oxygen reduction reaction (ORR) occurred at the platinum catalyst and within the biofilm. Although the EPS was not specifically considered in the biofilm simulation, the fraction of EPS in the biofilm was used to correct the biofilm porosity. To simulate the experimental procedure of refreshing the growth medium, the bulk liquid was assumed to be reset to initial conditions every 2 days. The suspended biomass growth and its effects were also considered in this model, including the interface and exchange between the bulk liquid and cathode biofilm. Since the bulk liquid was reset every 48 hours, the suspended biomass concentration also reverted to the initial amount, shown in Table 1.

2.2. Model reactions analysis

The cathode was comprised of multiple layers, each with distinct physical properties, and each layer was assumed to have discrete boundaries; such an assumption was employed to greatly simplify the less-defined interfaces between cathode layers in a real MFC cathode. The cathode reactions were assumed to all occur either in the catalyst layer or biofilm. Because AAB were present in the cathode biofilm as well as a metallic catalyst, electron distribution between

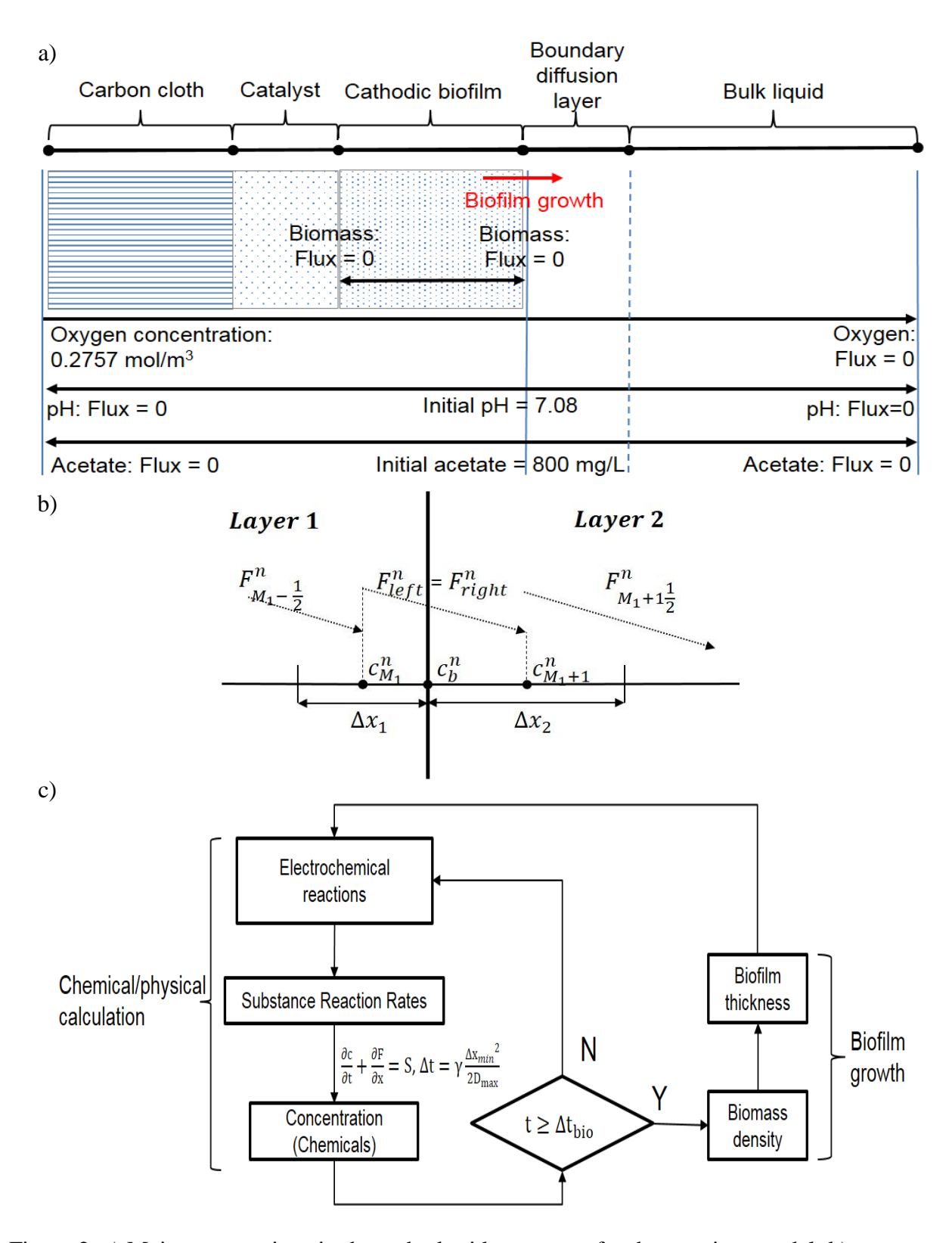


Figure 2. a) Major assumptions in the cathode side structure for the transient model; b) Schematic of boundary between two layers; c) Hybrid step times for the chemical substance and biofilm growth calculation in model.

the two sinks were included in the model. The ORR in the catalyst layer is purely electrochemical and it was assumed that no free cations participated in the ORR reaction. The expected ORR on platinum is production of hydroxyl from oxygen and water [6]:

$$0.250_2 + e^- + 0.5H_2O \rightarrow OH^-$$
 (1)

Marcus et al. [17] systematically analyzed the double Monod equation and established the overpotential-substrate double Monod equation. This relationship was used to describe the reaction rate calculations in both the catalyst layer and cathode biofilm. Eqn. (2) gives the oxygen reaction rate in the catalyst layer:

$$r_{O_2,cl} = -q_{O_2, \max} \frac{c_{O_2}}{K_{O_2} + c_{O_2}} \frac{1}{1 + \exp(-\frac{F}{PT} \eta_{act} + \frac{F}{PT} \eta_K)}$$
(2)

where $r_{O2,cl}$ is oxygen reaction rate in the catalyst layer (mg/L·s), $q_{O2,max}$ is the maximum specific rate of oxygen consumption (mg O_2/L ·s), c_{O2} is the oxygen concentration (mg/L), K_{O2} is the half-max-rate oxygen concentration (mg/L), η_{act} is the cathode activation overpotential (mV), η_K is the cathode half-max overpotential (mV), F is the Faraday constant, T is the temperature, and R is the ideal gas constant. Hydroxide production rate can also be derived from $r_{O2,cl}$:

$$r_{OH,cl} = -4 \frac{r_{O_2,cl}}{M_{O_2}} \times 0.001 \frac{g}{mg}$$
 (3)

where $r_{O2,cl}$ is the hydroxide production rate (mg/L·s), and M_{O2} is the oxygen molar mass (g/mol).

In the cathode, the AAB growth rate is assumed to be dependent on O₂ concentration. The cathode serves as the electron donor, thus there is no donor reaction specified for the AAB. The AAB is considered a biocatalyst and competes with the metal catalyst to accept electrons [9]; however, the AAB electron consumption is less than 10 % of the metal catalyst rate [10]. In addition, the method of accepting electrons for the AAB is still unknown [3]. In the transient model, the initial percentage of AAB in the biofilm was assumed to be 15 % and was allowed to

change with the biofilm growth. In the steady-state model, it was assumed that the AAB concentration percentage is at 15 %. Eqn. (4) shows the biomass cell synthesis reaction in biofilm:

$$\frac{1}{5}CO_2 + \frac{1}{20}HCO_3^- + \frac{1}{20}NH_4^+ + \frac{11}{20}H_2O + e^- \rightarrow \frac{1}{20}C_5H_7O_2N + OH^-$$
 (4)

Eqn. (5) gives the oxygen reaction rate calculation:

$$r_{O_{2},AAB} = -q_{O_{2},AABmax} X_{AAB} \frac{c_{O_{2}}}{K_{O_{2},AAB} + c_{O_{2}}} \frac{1}{1 + \exp(-\frac{F}{RT}\eta_{act} + \frac{F}{RT}\eta_{K})}$$
(5)

where $r_{O2,AAB}$ is AAB oxygen reaction rate (mg/L·s), $q_{O_2,AABmax}$ is AAB maximum specific rate of oxygen consumption (mg O₂/mg AAB·s), X_{AAB} is the AAB concentration (mg/L). Other reaction rates can be calculated from $r_{O2,AAB}$:

$$r_{OH,AAB} = -Y_{OH} \frac{r_{O_2,AAB}}{M_{OH}} \tag{6}$$

$$r_{AAB} = -Y_{AAB}r_{O_2,AAB} - b_{decay}X_{AAB}$$
 (7)

where $r_{OH,AAB}$ is the hydroxide reaction rate (mM/s) from AAB, Y_{OH} is the hydroxide yield (mol OH⁻/mol O₂), r_{AAB} is the AAB reaction rate (mg/L·s), Y_{AAB} is the biomass yield (mg AAB/mg O₂), b_{decay} is the decay rate (s⁻¹), and X_{AAB} is the AAB concentration in biofilm (mg/L).

The AAB are a relatively small population of biomass compared to the HAB that are present in the cathode. Eqn. (8) gives the reaction for acetate oxidization by the HAB. The electrons are utilized for biomass synthesis as well as endogenous respiration; the biomass synthesis reaction is shown in Eqn. (4).

$$\frac{1}{8}CH_3COO^- + \frac{3}{8}H_2O \to \frac{1}{8}CO_2 + \frac{1}{8}HCO_3^- + H^+ + e^-$$
 (8)

The utilization of acetate by the HAB is affected by the biomass concentration as well as acetate and oxygen concentrations. The equation for acetate reaction rate, based on the double Monod

equation, is shown in Eqn. (9). Eqn. (10) gives the equation for HAB acetate consumption rate and Eqn. (11) gives HAB net growth rate (the sum of HAB gross growth rate and decay rate):

$$r_{Ac,HAB} = -q_{Ac, HABmax} X_{HAB} \frac{c_{O_2}}{K_{O_2,AAB} + c_{O_2}} \frac{c_{Ac}}{K_{Ac,AAB} + c_{Ac}} \frac{1}{1 + \exp(-\frac{F}{PT}\eta_{act} + \frac{F}{PT}\eta_K)}$$
(9)

$$r_{O_2,HAB} = -Y_{O_2,HAB}r_{Ac,HAB}$$
 (10)

$$r_{HAB} = -Y_{HAB}r_{Ac,HAB} - b_{decay}X_{HAB}$$
 (11)

where $r_{Ac,HAB}$ is HAB acetate reaction rate (mg/L·s), $q_{Ac,HABmax}$ is HAB maximum specific rate of acetate consumption (mg Ac/mg HAB·s), X_{HAB} is the HAB concentration (mg/L). $r_{O2,HAB}$ is the oxygen reaction rate (mg/L·s) by HAB, $Y_{O2,HAB}$ is the oxygen reaction rate (mg O₂/mg Ac), r_{HAB} is the HAB reaction rate (mg/L·s), Y_{AAB} is the biomass yield (mg HAB/mg Ac).

2.3. Model mass balance

In the air-cathode MFC reactor, oxygen diffuses from air through the cathode structure into bulk liquid in both gas and liquid phases. Henry's law, shown in Eqn. (12), is used to describe the equilibrium between dissolved oxygen and gaseous oxygen at the PTFE-carbon cloth interface [18].

$$H_{0_2,cc} = \frac{c_{0_2,gas}}{c_{0_2,aq}}$$
 (12)

where $c_{O2.aq}$ is the concentration of dissolved oxygen (mg/L), $c_{O2,gas}$ is the concentration of gaseous oxygen (mg/L), and $H_{O2,cc}$ is the Henry's law constant (dimensionless).

For mass transport in the cathode, a transient mass balance is the basis for both steady state and transient state models, as shown in Eqn. (13):

$$\frac{\partial c_i}{\partial t} = D_i \frac{\partial^2 c_i}{\partial x^2} + r_i \tag{13}$$

where i is a dissolved species in the cathode, c_i is the concentration of species i, D_i is the effective diffusion coefficient, and r_i is the reaction rate of species i for each mobile species.

The explicit finite volume method was used as the computational method for the modeling calculations. Concentrations are calculated at discrete control volumes on a meshed layer. Eqn. (13) can be approximated, as shown in Eqn. (14):

$$c_k^{n+1} = c_k^n + \frac{\Delta t}{\Delta x} D(F_{k-1/2}^n - F_{k+1/2}^n) + r_k^n, \quad k = 1, 2, \dots, M$$
 (14)

where k is the sequence number for the control volume, n is the iteration, Δt is the step time, Δx is the length of the control volume, F is mass flux, and M is the total number of the control volume. Because each species diffuses from layer to layer, the concentration calculation must be solved between each layer. As shown in Fig. 2 b), the concentration flux at a control volume boundary can be calculated as shown in Eqns. (15) and (16).

$$F_{\text{left}}^{n} = D_{1} \frac{c_{b}^{n} - c_{M_{1}}^{n}}{\Delta x_{1}}$$
 (15)

$$F_{\text{right}}^{n} = D_{2} \frac{c_{M_{1}+1}^{n} - c_{b}^{n}}{\Delta x_{2}}$$
 (16)

where c_b is the boundary concentration, M_1 is the serial number of a control volume, and Δx_1 and Δx_2 are the length of control volumes in Layer 1 and Layer 2. Since mass is conserved, the flux at the boundaries does not change. Therefore the equations for calculating concentration as well as boundary flux can be shown in Eqns. (17) and (18).

$$c_b^n = \frac{\Delta x_2 D_1 c_{M_1}^n + \Delta x_1 D_2 c_{M_1+1}^n}{\Delta x_1 D_2 + \Delta x_2 D_1}$$
(17)

$$F_{M_1 + \frac{1}{2}}^n = F_{left}^n = F_{right}^n = -D_2 \frac{c_{M_1 + 1}^n - c_b^n}{\frac{1}{2}\Delta x_2}$$
 (18)

2.4. Model electron balance

Electron transfer in the biofilm has been extensively investigated, yielding several theories to describe the mechanisms by which electrons are transferred from the microbes to an electrode; these include chemical shuttles produced by microorganisms, protein nanowires, and chemically active redox enzymes added from an external source [19]. Recent research has considered the conductivity of the biofilm itself found at the anode and cathode [17, 20, 21]. Despite uncertainty regarding the mechanism for electron transfer in the biofilm, the cathode current can be simulated based on the electrochemical equations for the cathode biofilm and cathode catalyst layer, as shown in Eqns. (19) and (20).

$$0 = \frac{\partial i_{cl}}{\partial x} + \frac{\gamma_{cl} Fr_{O_2, cl}}{M_{O_2}}$$
 (19)

$$0 = \frac{\partial i_{bio}}{\partial x} + \frac{\gamma_{bio} Fr_{O_2, AAB}}{M_{O_2}}$$
 (20)

where i is the current density (A/m^2) , γ is the electron equivalence (mol e⁻/mol O₂). The total current is the sum of the current density in the biofilm and catalyst layers, as shown in Eqn. (21).

$$I = (\int i_{cl} dx + \int i_{bio} dx) S_{area}$$
 (21)

where, I is the current from the external circuit into the cathode and S_{area} is the geometric cathode area (m^2).

In experiments, the microbial fuel cell was connected to an external resistance (R_{ext}), and the cell voltage was calculated based on Eqn. (22) when the current was measured for a particular resistor.

$$V_{\text{cell}} = IR_{\text{ext}}$$
 (22)

It is noted that, due to voltage losses, the actual voltage measured for an MFC is less than the theoretical value at open circuit and any operating current. The voltage losses are roughly divided into activation overpotential η_{act} , concentration overpotential η_{con} , and ohmic overpotential η_{ohm} .

These three overpotentials dominate at different current densities: activation overpotential in the low-current region, ohmic overpotential at moderate cell current, and concentration overpotential at the highest current densities achieved by a system [18]. In an MFC, the operating voltage can be described as the departure from equilibrium voltage caused by the various overpotentials:

$$V_{\text{cell}} = (E_{\text{C}}^{0} - |\eta_{\text{C,act}}| - |\eta_{\text{C,con}}|) - (E_{\text{A}}^{0} + |\eta_{\text{A,act}}| + |\eta_{\text{A,con}}|) - |\eta_{\text{ohm}}|$$
(23)

where E_C^0 is the cathode equilibrium voltage (mV), E_A^0 is the anode equilibrium voltage (mV). The ohmic overpotential is calculated by Eqn. (24).

$$|\eta_{\text{ohm}}| = I(R_A + R_{BL} + R_C) \tag{24}$$

where R_A is the electronic resistance of the anode, R_{BL} is the ionic resistance of bulk liquid, and R_C is the electronic resistance of cathode. Development of a concentration gradient, when electrochemical current is comparable to mass transport rate, leads to concentration overpotential [18], described in Eqn. (25).

$$\eta_{\text{con}} = \frac{RT}{4F} \ln \left(1 - \frac{i}{i_{\text{o,c}}} \right) \tag{25}$$

where $i_{0,C}$ is the limiting cathode current density [18].

Because this work only simulated the cathode in a MFC reactor, experimental anode potentials were used as E_A in the Eqn. (26).

$$E_{A} = E_{A}^{0} - \left| \eta_{A,act} \right| - \left| \eta_{A,con} \right| - IR_{A}$$
 (26)

By combining Eqns. (22) and (23), activation overpotential in the cathode can be described as a function of current and equilibrium potentials.

$$\left| \eta_{\text{C,act}} \right| = E_{\text{C}}^{0} - I(R_{\text{ext}} + R_{\text{bl}} + R_{\text{C}}) - \frac{RT}{4F} \lg \left(1 - \frac{i}{i_{\text{o,c}}} \right) - E_{\text{A}}$$
 (27)

The above equations were used to simulate the air cathode MFC, written in C++ then implemented on a Linux system on the Newton – a high performance computer at the University

of Tennessee. Both electrochemical and biochemical reactions were defined based on their stoichiometry and rate parameters developed in previous work [10].

2.5. Model Strategies

In the steady state model, external resistance was the controlling parameter used to calculate all other results. The simulation time required to obtain the concentration of dissolved species in the cathode and current generation as a function of external resistance was 40 ~ 60 mins. In the transient simulation, the concentration distribution was simulated in both the cathode and bulk liquid; the biofilm density and suspended biomass growth were both simulated. The transient model simulated 15 days of MFC operations, requiring approximately 18 hours of computational time. In order to enable the simulation in a reasonable time (<24 hours), OpenMP with variable time scale optimization was utilized.

OpenMP is a parallel computation method that utilizes multiple computational threads simultaneously. Although OpenMP has shared memory, it can only successfully use multiple threads when each thread calculation is independent of the calculations occurring on other threads. One advantage of OpenMP is that it avoids message transfer in different, separated memories and simplifies the coding design [22]. Because of these features, OpenMP was applied to the transient model. In the substance concentration calculation, the reaction rate for different substances in the MFC reactor were computed separately in different threads and the mass transport calculation for different substances was also distributed across several threads for calculation.

The MFC reactions and transport processes occur at very different time scales [23]; consideration of the time scales in the transient cathode model was helpful to increase computational efficiency. The order of magnitude of the characteristic times for molecular

diffusive transport, biomass growth, biomass decay, and detachment are presented in the Table 1. The magnitude of the diffusion coefficients in liquid are in the range of 10^{-9} - 10^{-11} , while the magnitude of the biofilm detachment coefficient was 10^{-2} . The processes that impact the biofilm thickness are much slower than the mass transport of chemical substances [24]. If there is only one time scale in the transient model, the smallest chemical time scale must be satisfied [25], determined by the calculation shown in Eqn. (28).

$$\Delta t = \gamma \frac{\Delta x_{min}^2}{2D_{max}} \tag{28}$$

where Δt is the simulation step time (s), $\gamma = 0.95$ which is the convergence factor (dimensionless), Δx_{min} is the smallest control volume in the model (m), and D_{max} is the largest diffusion coefficient (m²/s). Because the biomass density and biofilm growth components change relatively slowly, they do not need to be computed in every time step associated with transport or chemical reaction. Therefore, the biofilm growth time step (Δt_{bio}) was adopted in the algorithm. As shown in Fig. 2 c), biofilm growth computation wasn't executed unless Δt_{bio} was exceeded. The biofilm step time was assumed to be 5 mins in the simulation. By incorporating OpenMP and the separate chemical/biological time scales into the cathodic transient model, computational time was reduced from days to hours.

Table 1. Model parameters for cathode simulation.

Name	Description	Values	Unit
b _{decay}	Biomass decay rate ^a	3.00×10 ⁻⁶	1/s
c _{Ac,0}	Initial Concentration, sodium acetate ^b	800	mg/L
	Boundary concentration, gaseous		
$c_{\mathrm{O2,g}}$	oxygen ^b	237.66	mg/L
	Reference concentration in reactor,		
CO2,ref	oxygen	3.79	mg/L
$D_{\text{Ac},\text{liq}}$	Diffusion coefficient in liquid, acetate ^c	1.21×10^{-9}	m^2/s
$D_{\text{bio},\text{liq}}$	Diffusion coefficient in liquid, biomass	$1.50\times10^{\text{-}11}$	m^2/s
	Diffusion coefficient in liquid,		
$D_{\text{OH},liq}$	hydroxide ^d	4.59×10^{-9}	m^2/s
D _{O2-He}	MS diffusivity, O ₂ -He component ^c	8.60×10^{-5}	m^2/s
D_{O2-N2}	MS diffusivity, O ₂ -N ₂ component ^c	2.30×10^{-5}	m^2/s
$D_{O2,liq}$	Diffusion coefficient in liquid, oxygen ^c	2.10×10^{-9}	m^2/s
$\mathrm{E_{C}}^{0}$	Cathode equilibrium voltage ^c	552	mV
F	Faraday constant ^c	96485	C/mol
H_{N2}	Henry constant, nitrogen ^c	1.66×10^5	J/mol
H_{O2}	Henry constant, oxygen ^e	7.79×10^4	J/mol
$i_{ m lim}$	Limit current density	2.5	A/m^2
\mathbf{k}_{det}	Biofilm detachment coefficient	1.00×10^{-2}	g/m ⁴ ·s
	Half-max-rate acetate concentration,		
K_{AcH}	heterotrophic biomass	150	mg/mol

	Half-max-rate oxygen concentration in		
K_{O2}	cathode	0.128	mg/L
	Half-max-rate oxygen concentration,		
K_{O2A}	autotrophic biomass	1.28	mg/L
	Half-max-rate oxygen concentration,		
$K_{\rm O2H}$	heterotrophic biomass	1.28	mg/L
$\mathcal{L}_{ ext{bio}}$	Initial length, cathode biofilm	0.01	mm
L_{bl}	Length, bulk liquid ^c	39.0	mm
L_{bdl}	Length, boundary diffusion layer ^c	0.5	mm
L_{cc}	Length, carbon cloth ^c	0.18	mm
L_{cl}	Length, Pt/C catalyst layer ^c	0.032	mm
L_{pdl}	length, PTFE diffusion layer ^c	0.023	mm
pH_0	pH in bulk liquid	7.08	\
P_0	Gas pressure ^c	1.01×10^5	Pa
	Maximum specific rate of acetate		
q _{max} .AcH	utilization ^f	5.56×10^{-5}	(mg Ac)/(mg HAB·s)
	Maximum specific rate of acetate		
qmax.Acsus	utilization	5.56×10^{-6}	(mg Ac)/(mg SUS·s)
	Maximum specific rate of oxygen		
q _{max.O2}	utilization	1.46×10^{-7}	g/L·s
	Maximum specific rate of oxygen		
qmax.AcA	utilization, autotrophic biomass	8.64×10^{-6}	$(mg\ O_2)/(mg\ AAB\cdot s)$
R	Gas constant	8.314	J/mol·K

$S_{cathode}$	Cathode's cross sectional area in MFC ^c	7.07×10^{-4}	m ²
T	Temperature	303.15	K
	Initial concentration in biofilm, total		
$X_{\rm bio 0}$	biomass	3.0	g/L
	Initial suspended concentration in liquid,		
X_{sus0}	total biomass	0.005	g/L
$\epsilon_{ m bio}$	Porosity, biofilm	0.95	\
ϵ_{cc}	Porosity, carbon cloth ^c	0.75	\
$\epsilon_{ m cl}$	Porosity, Pt/C catalyst layer ^c	0.30	\
ϵ_{pdl}	Porosity, PTFE diffusion layers	0.10	\
η_{K}	Cathode half-max overpotential	240.028	mV
ρы	Density, bulk liquid ^c	1.05	g/cm ³
$ ho_{ m bio}$	Density, bacteria	1.54	g/cm ³
σ	Mass fraction of HAB in biofilm	0.85	\
Obio	Conductivity, cathode biofilm	0.1	S/m
σ_{bl}	Conductivity, bulk liquid ^c	0.755	S/m
σ_{cc}	Conductivity, carbon cloth	1.00×10^5	S/m
$\sigma_{ m cl}$	Conductivity, Pt/C catalyst layer	1.00×10^3	S/m

Values for the other model parameters were assumed based on common practical experience.

a from Reference [26].

b from experimental data.

c from Reference [27].

d from Reference [28].

Final Manuscript Version

e from Reference [18].

f from Reference [29].

3. Model results and evaluation

3.1. Comparison of the performance of nitrox and heliox as the gas source for air cathode MFC system

Experimental polarization and power density curves were compared for different cathode atmospheres as shown in Fig. 3 a) [16]. The same flow of nitrox (composed of 79 % N₂ and 21 % O₂) and heliox (composed of 79 % He and 21 % O₂) was employed. The gas flows for both nitroxfed and heliox-fed reactors were controlled to result in identical gaseous oxygen concentration (c_{O2.g}) on the MFC cathode surface, as assumed in Table 1. As shown in Fig. 3, the heliox-fed reactor produced slightly more power than the nitrox-fed MFC reactor. The air-fed reactor was passively exposed to air, thus the markedly higher power density yielded by the nitrox/heliox reactors is predominately due to higher gas pressure and improved mass transport; in addition to greater power density, the nitrox/heliox performance was more stable than the passive air reactor. The maximum power density produced by the heliox MFC was 1320 ± 50 mW/m² at 75 Ω external resistance, while the nitrox-fed MFC reached a maximum power of $1280 \pm 50 \text{ mW/m}^2$, and the air-fed MFC showed the lowest maximum power at $1050 \pm 40 \text{ mW/m}^2$. The maximum difference in power density between heliox and nitrox was 95 W/m² at 50 Ω external resistance. Comparing the power density curves, the maximum percentage difference is 9.0 %. In all cases, individual electrode potentials were recorded against a reference electrode; the cathode overpotential was always much greater than the anode overpotential.

While the performance difference between the nitrox-fed reactor and heliox-fed reactor was small in experiments, it was also consistent and reproducible. A possible explanation is that oxygen transport and reactions under these two different mixture gases is slightly different. The diffusion

coefficient of oxygen is 8.6×10^{-5} m²/s in helium at the experimental conditions, compared to 2.3×10^{-5} m²/s in nitrogen, which allows oxygen to diffuse more rapidly into the

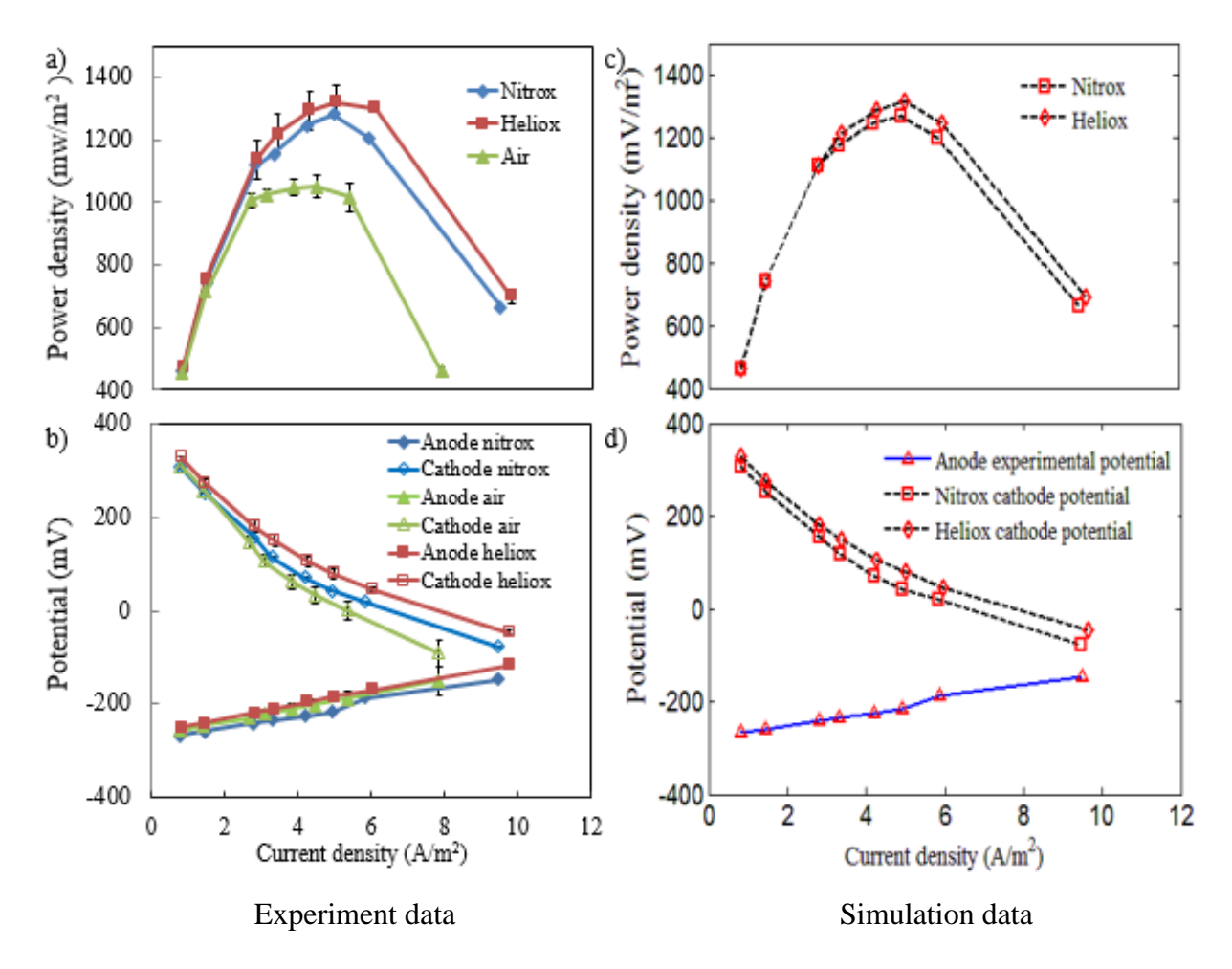


Figure 3. Experimental results for nitrox-fed, heliox-fed and air-fed MFCs: a) power density curves; b) polarization curves; steady state simulation results for nitrox-fed, and heliox-fed MFCs: c) power density curves; d) polarization curves.

gas phase in the cathode, enabling a small performance gain over nitrox. The calculation of binary gas-phase diffusion coefficients is shown in Eqn. (29),

$$D_{12}\left(\frac{m^2}{s}\right) = \frac{a}{P}\left(\frac{T}{\sqrt{T_1 T_2}}\right)^b (P_1 P_2)^{1/3} (T_1 T_2)^{5/12} \left(\frac{1}{M_1} + \frac{1}{M_2}\right)^{1/2}$$
(29)

where, D_{12} is the diffusion coefficient of species 1 into species 2, temperature T is in Kelvin and pressure P is in atmosphere. For a nonpolar gas pair, a and b are 2.745×10^{-8} and 1.823, respectively [30]. Diffusion of oxygen into the liquid that floods the carbon cloth does not account for the observed performance difference; however, inclusion of a small volume of gas in the mostly-flooded cathode layer provides enough oxygen to support the results observed. To achieve the performance difference between nitrox and heliox observed experimentally, the simulated carbon cloth layer required 3 % gas phase and the catalyst included 1 % gas phase by volume.

In the cathodic steady state simulation, it was assumed that there were three phases in the diffusion media (carbon cloth domain and Pt/C catalyst domain): solid (carbon cloth), liquid (growth medium) and gas (air, heliox, or nitrox). The cathode structure and compression define the porosity of the diffusion media. It was assumed that the oxygen is only gas phase in PTFE domain. Oxygen was assumed to be able to diffuse in both the liquid and gas, noting that all oxygen was able to be fully dissolved at the carbon cloth – Pt/C layer interface. The 1-D diffusion equation in the carbon cloth is shown in Eqn. (30) [31].

$$\theta \frac{\partial c_{\text{liq}}}{\partial t} + a_{\text{v}} \frac{\partial c_{\text{gas}}}{\partial t} = \nabla^2 D_{\text{liq}} c_{\text{liq}} + \nabla^2 D_{\text{gas}} c_{\text{gas}}$$
(30)

where θ is the liquid pore fraction in the carbon cloth (dimensionless), a_v is the gas pore fraction in the carbon cloth (dimensionless), c_{gas} and D_{gas} are the oxygen gas phase concentration (mol/m³) and effective diffusion coefficient (mol/m²·s), and c_{liq} and D_{liq} are the oxygen liquid phase concentration (mol/m³) and effective diffusion coefficient (mol/m²·s), respectively. The gas

effective diffusion coefficient and liquid effective diffusion coefficient can be calculated as shown in Eqns. (31) and (32).

$$D_{liq} = \theta \pi_L D_L \tag{31}$$

$$D_{gas} = a_v \pi_G D_G \tag{32}$$

where π_L and π_G are the liquid and gas tortuosity (dimensionless), D_L and D_G are the liquid and gas diffusion coefficients (mol/m²·s). Eqn. (12) can be substituted into Eqn. (30), yielding Eqn. (33).

$$\left(\theta + \frac{a_{v}}{H_{i}}\right) \frac{\partial c_{liq}}{\partial t} = \nabla^{2} \left(D_{L} + \frac{D_{G}}{H_{i}}\right) c_{liq}$$
(33)

Then, Eqns. (31) and (32) can be substituted into Eqn. (33) to obtain Eqn. (34), which described oxygen mass transport in the cathode.

$$\left(\theta + \frac{a_{v}}{H_{i}}\right)\frac{\partial c_{L}}{\partial t} = \nabla^{2}\left(\theta\pi_{L}D_{L} + \frac{a_{v}\pi_{G}D_{G}}{H_{i}}\right)c_{L}$$
(34)

The cathodic steady state model was evaluated at external resistances of: 10Ω , 50Ω , 75Ω , 100Ω , 150Ω , 200Ω , 500Ω , and 1000Ω . The measured anodic potentials for the external resistance settings are presented in Table 2. With the above considerations regarding oxygen diffusivity in nitrogen and helium, simulated power density and polarization curves are shown in Fig. 3 c) and d). The simulated maximum power density produced by the heliox reactor is 1314 mW/m^2 at 75Ω external resistance, while the nitrox reactor achieves a maximum power of 1269 mW/m^2 at 75Ω external resistance. The simulated maximum difference in power density is 45 mW/m^2 at 50Ω external resistance. Comparing the simulated power density curves, the maximum percentage difference is 3.6 %. The simulation results in Fig. 3 c) and d) show that the simulation results accurately describe experimental data in both power density and cathode potentials. It is noted that the two simulated power density curves for nitrox and heliox are slightly closer to each

other than they were in the experiments, but this difference is relatively small and within experimental error.

In addition to the electrochemical results, the distribution of species such as hydroxide in the cathode was simulated in the steady state model to shed light on the ORR. Fig. 4 shows the calculated pH distribution in the cathode for heliox-fed and nitrox-fed MFC reactors. The cathode pH in the heliox MFC was consistently higher than that of the nitrox reactor, indicating more rapid oxygen reduction since hydroxide is the product of the ORR. The slope of the pH profile is steeper in the Pt/C catalyst layer than in the biofilm, indicating that the ORR reaction rate in the Pt/C catalyst layer is faster than in the biofilm. As shown in Fig. 4, the pH of the boundary layer is constrained to 7.08 for the steady state model. It should be noted that a limitation of the current model is that there is no feedback between elevated cathode pH and the biomass or catalyst reactions.

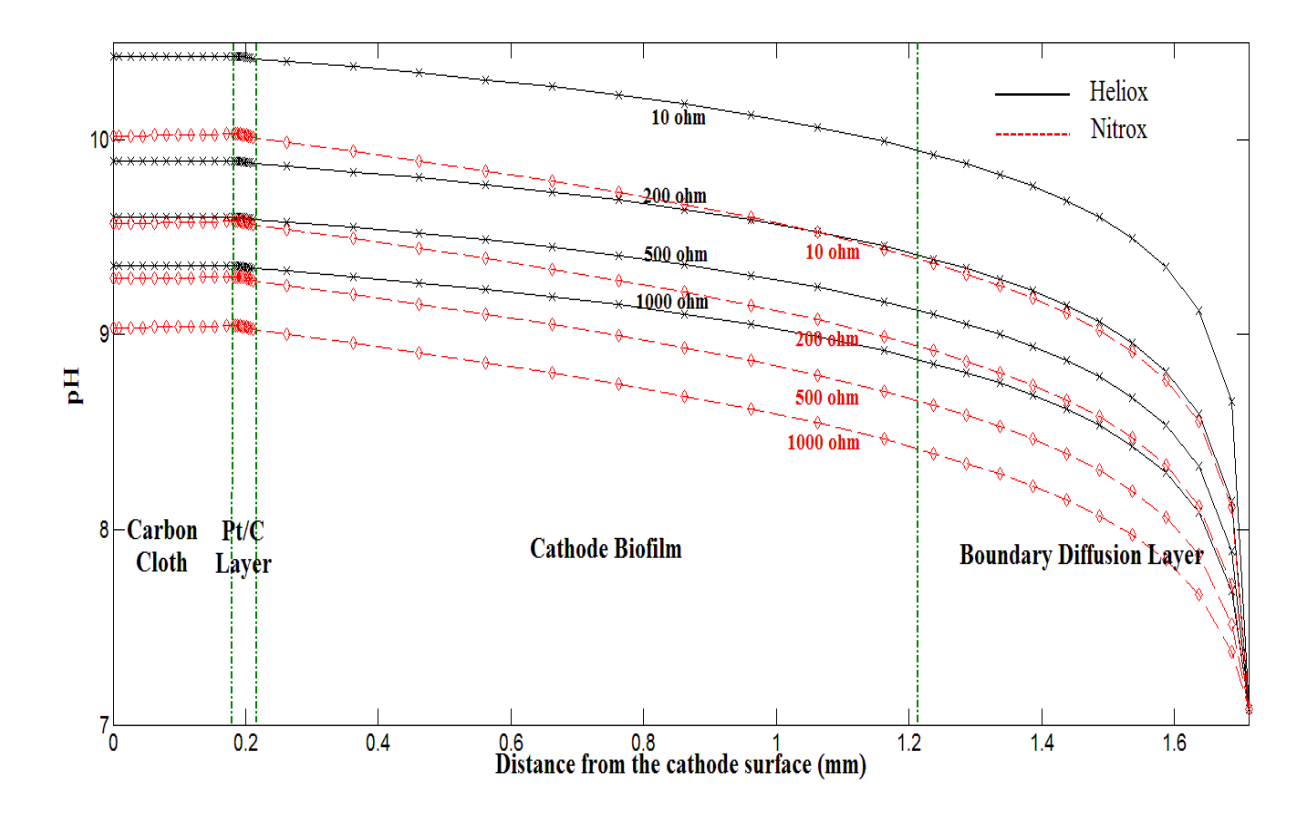


Figure 4. Simulation results of pH distribution in cathodic side for nitrox-fed and heliox-fed MFCs.

Table 2. The anode potential values in different external resistors.

External resistor (Ω)	Anode potential (mV) vs.
	Ag/AgCl
10	-147.79
50	-186.13
75	-217.27
100	-225.32
150	-234.96
200	-242.19
500	-259.51
1000	-266.60

3.2 Cathode transient model analysis

The cathode transient model focuses on species changes (e.g. biomass, acetate and hydroxide) and the effects of environmental changes on the biomass (AAB, HAB in the cathode biofilm and suspended biomass). Side-reactions that may impact the electrode or membrane materials are not considered in the transient model. A simulation period of 15 days from inoculation was assumed since experimental cells generally achieved stable performance in this time period. Based on experimental measurements, the range of initial dissolved oxygen (D.O.) across many cell builds was 2.9 - 4.2 mg/L, thus D.O. was set to 4.2 mg/L. Fig. 5 shows the cathodic biofilm thickness growth and average acetate concentration and D.O. in the reactor over 15 days. In Fig. 5 a), the biofilm required almost one week to achieve fully grown thickness approaching 1 mm, which agrees with the cathodic biofilm thickness range observed experimentally. Upon reaching a

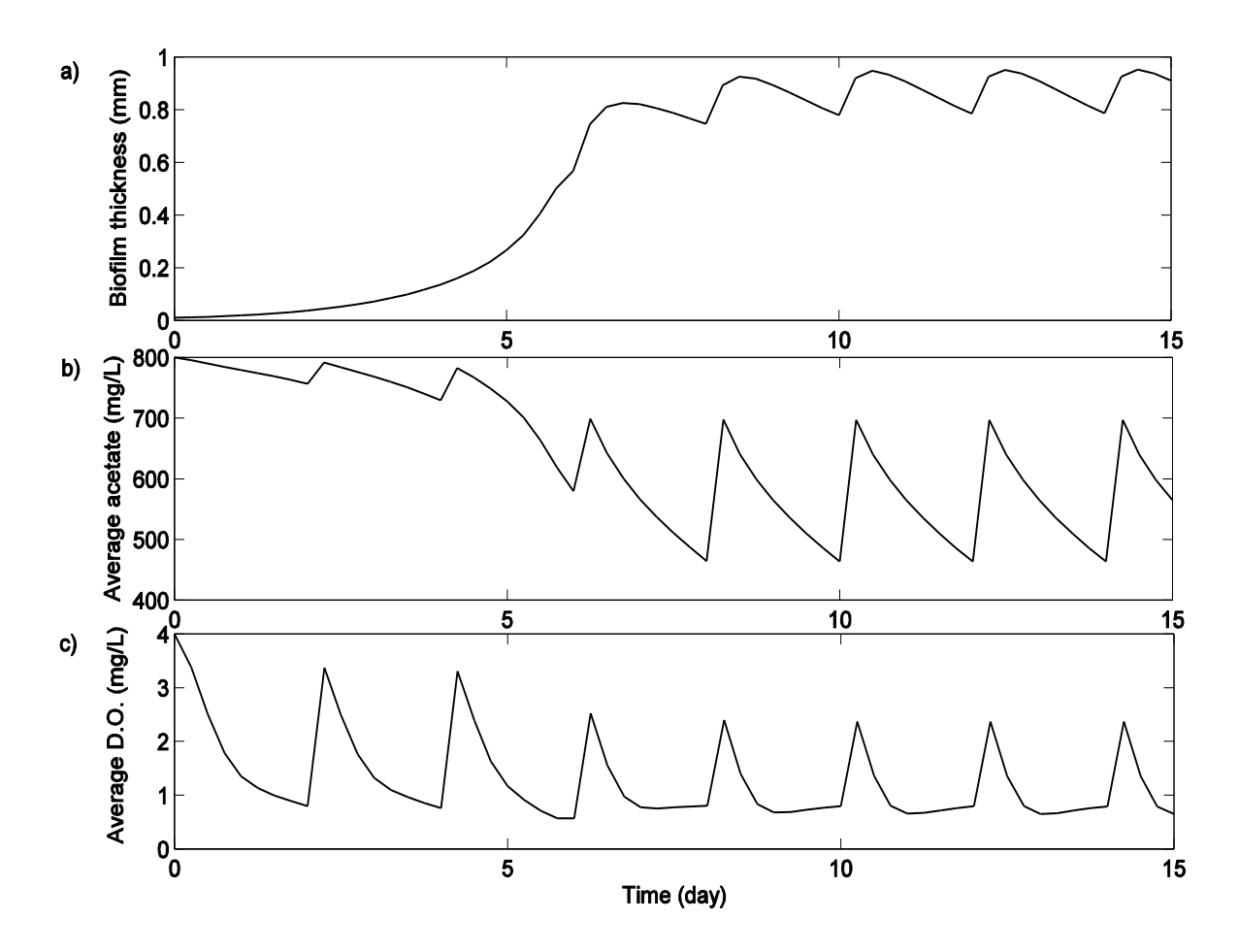


Figure 5. Simulation results for cathodic biofilm thickness and average D.O. (dissolved oxygen) in bulk liquid over 15 days: a) Cathodic biofilm thickness; b) average acetate concentration in the reactor; c) average D.O. in the reactor.

stable, maximum biofilm thickness, the biofilm thickness fluctuated with acetate concentration, as shown in Fig. 5 b). Two days after each bulk liquid refreshment, most of the acetate was consumed resulting in decreased biomass growth rate as the acetate concentration reached a minimum. As is apparent in Fig. 5 c), D.O followed a similar trend, reaching maxima upon each bulk liquid replacement. It can be seen in Fig. 5 a) and Fig. 5 c) that the D.O. actually increased slightly over every 2 day cycle from day 8 onward. The anodic biomass functions only in an anaerobic environment, thus it is beneficial for the one chamber MFC system to maintain the lowest D.O. in the bulk liquid possible. Although the cathodic microorganisms compete with the anodic *exoelectrogens* for acetate, the cathodic biofilm and suspended biomass consume oxygen from the bulk liquid before reaching the anode.

The cathodic transient model simulated three types of biomass: HAB, AAB and suspended biomass. Fig. 6 shows the average density of the biomass over 15 days. In Fig. 6 a), the biomass densities of these three are compared. The HAB biomass dominated the biofilm population and its density followed the changes in acetate concentration; conversely, AAB growth was relatively stable and only comprised approximately 15 wt% in the cathodic biofilm. Because this simulation neglected the anode biofilm (which is much thinner than the cathode biofilm), the suspended biomass originates from the cathode detached biomass which then can grow in suspension. As shown in Fig. 6 c), the density of the suspended biomass decreased as the D.O. content decreased in the bulk liquid, but was always four orders of magnitude smaller than the biofilm biomass densities.

Fig. 7 shows the calculated distribution of the HAB/AAB biomass density in the cathodic biofilm over time. Biomass density increased rapidly, as did the biofilm thickness growth rate. In this simulation, the stable total biomass density was approximately 16.5 g/L - 18.0 g/L. Zhang

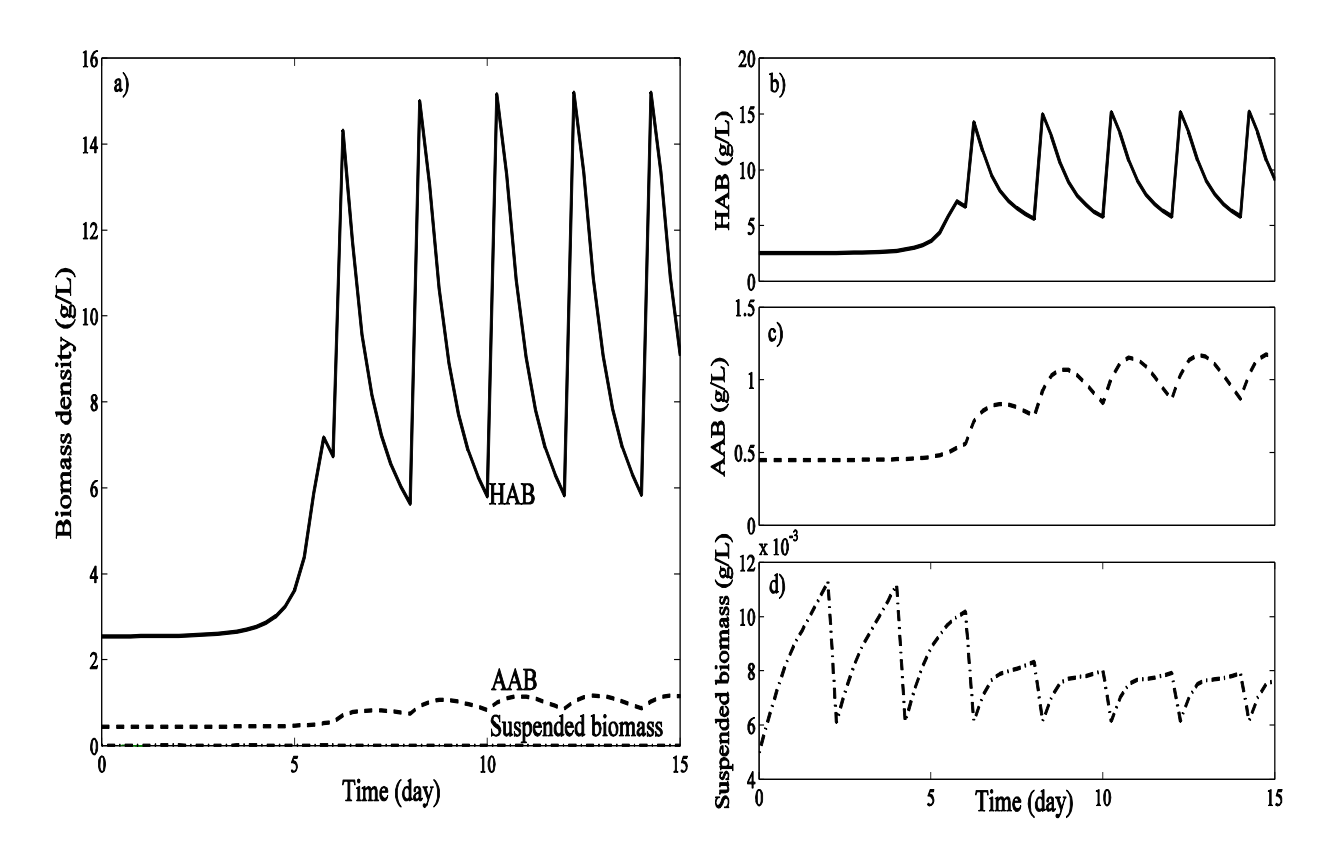


Figure 6. Simulation results for cathodic average HAB, AAB and average suspended biomass in bulk liquid over 15 days: a) average HAB concentration; b) average AAB concentration; c) average suspended biomass.

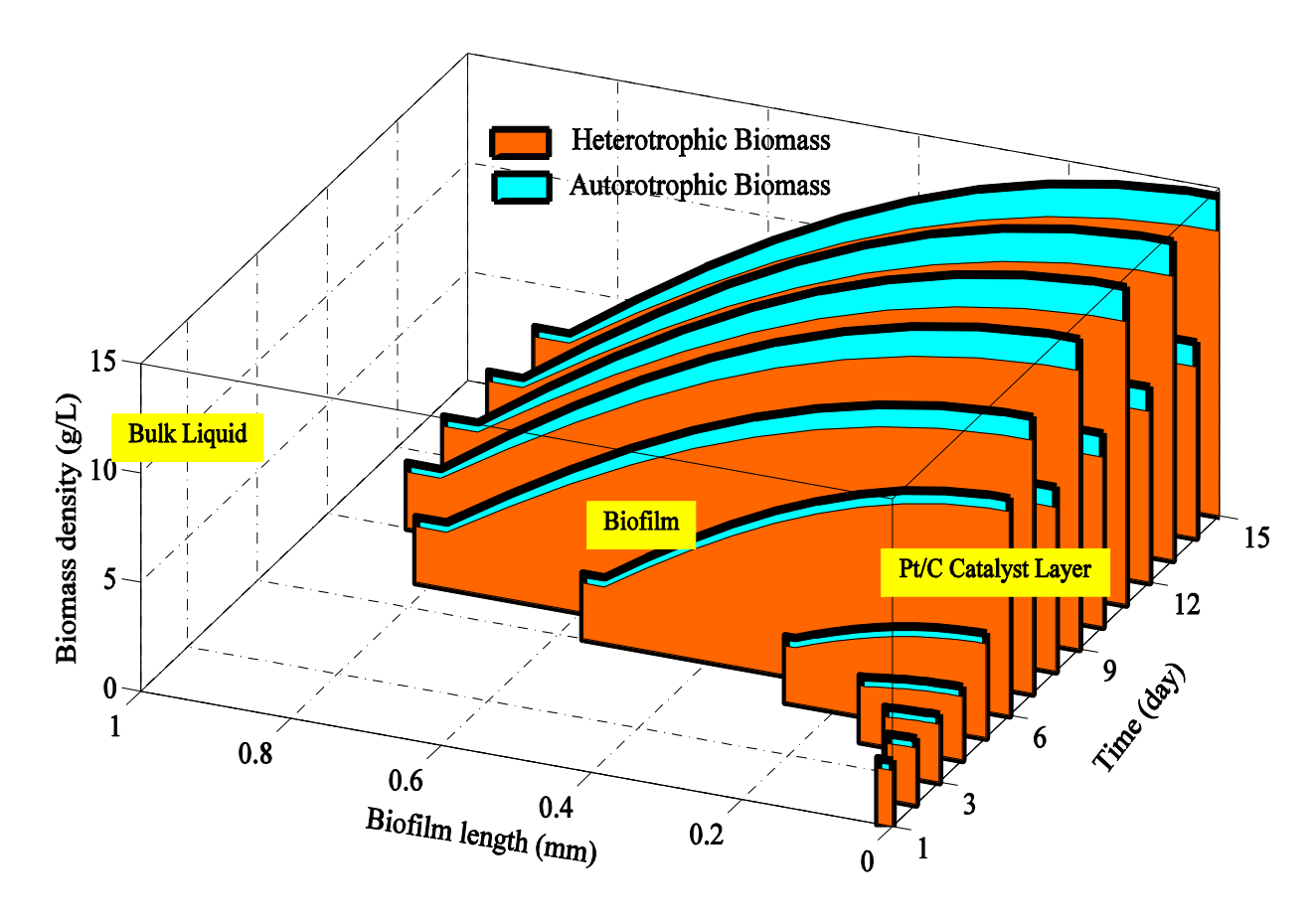


Figure 7. Simulation of AAB biomass density and HAB biomass density over 15 days.

and Bishop [32] measured biofilm density experimentally and found a range of 11.1 g/L – 107.8 g/L. The biofilm density depends on biofilm thickness, porosity, and biomass cultures, leading to the difference in the upper limit of biofilm density between this work and the experimental reference [32]. The acetate concentration in the reactor is greatly influenced by the cathodic biomass density and biofilm thickness as shown in Fig. 7. The simulation indicated that 92 % acetate consumption is by the cathodic biomass and 8 % acetate consumption is by the suspended biomass. The combined acetate consumption from anodic biomass, cathodic biomass and suspended biomass will be compared in the full cell model that is the subject of future work.

The transport and distribution of D.O. and acetate were also simulated across the cathode. In Fig. 8, the D.O. distribution is shown in different domains in 10 days simulation. The changes of the biofilm thickness are echoed by the biofilm thicknesses shown in Fig. 7. In Fig. 8, the distance from the last solid dot of the D.O. doted lines to the PTFE surface layer reflects the growth the cathodic biofilm thickness in every day. Oxygen was consumed most rapidly in the Pt/C catalyst layer, as indicated by the slope of the oxygen concentration profile. In absolute terms, more D.O. was consumed in the cathode biofilm, albeit at a slower rate, than in the Pt/C layer owing to its much greater thickness across the cathode.

4. Conclusions

A one-dimensional, multi-species, steady state model was constructed to explore the relationship between power density and electrochemical potentials. Experimental results were used to test the hypothesis that mass transport in the cathode strongly affects power output of an air cathode MFC. A heliox-fed MFC produced higher power than a nitrox-fed MFC (the maximum power output of heliox-fed reactor was 1314 mW/m², while the maximum power

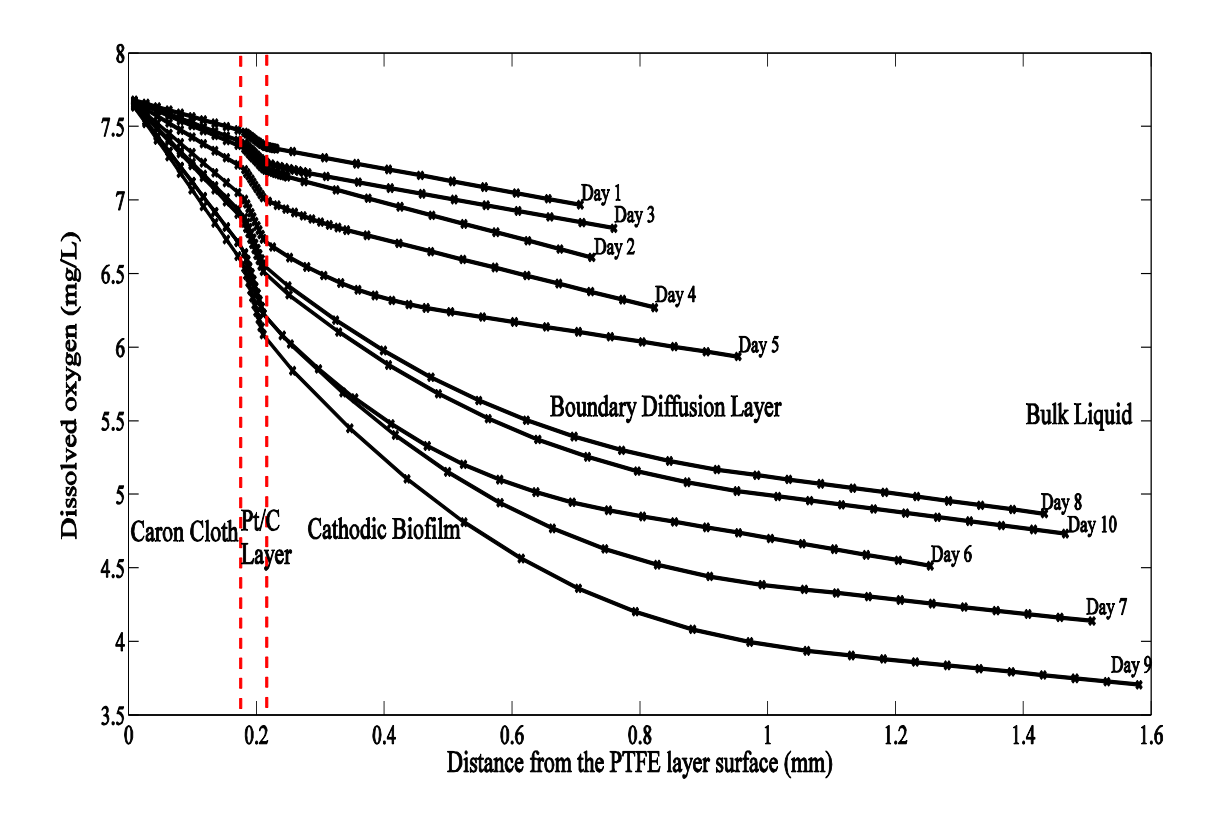


Figure 8. Simulation of the dissolved oxygen in cathodic side over 10 days.

output of the nitrox-fed reactor was 1269 mW/m².) Improved diffusion of oxygen in heliox, relative to nitrox, resulted enhanced oxygen reduction in the cathode. The persistent difference in performance between heliox- and nitrox-fed reactors led to simulating the existence of a gas phase in the assumed-flooded cathode. Based on simulation results, a small volume (3 % in the carbon cloth, 1 % in the catalyst layer) of gas phase in the cathode can result in the differences observed. Simulation results agree with experimental results that dominating overpotentials are from the cathodic part rather than the anodic part in the MFC; thus, greater improvement can be realized by optimizing the cathode of the single chamber, air cathode MFC.

In addition to the steady-state model, a one-dimensional, multi-species transient cathode-bulk liquid model was formulated; OpenMP with a modification for time scale optimization enabled timely computational requirements. It was found that heterotrophic, aerobic biomass dominate the cathode, with only ca. 15 % of the cathode biofilm present as autotrophic, aerobic biomass. The simulation compared well with overall cathodic biomass growth measurements and dissolved species distributions over time observed in experiments. The amount of oxygen-removing contribution and acetate consumption of the cathodic biomass and suspended biomass were able to be quantitatively compared by the transient model.

5. Acknowledgments

This research was supported by the US Army Research Office, contract number: W911NF-11-1-0531.

References

- [1] B.E. Logan, Microbial Fuel Cells, John Wiley & Sons, Inc., Hoboken, New Jersey, 2008.
- [2] H. Liu, R. Ramnarayanan, B.E. Logan, Environmental science & technology, 38 (2004) 2281-2285.
- [3] H. Rismani-Yazdi, S.M. Carver, A.D. Christy, O.H. Tuovinen, Journal of Power Sources, 180 (2008) 683-694.
- [4] Y. Yuan, S. Zhou, J. Tang, Environmental science & technology, 47 (2013) 4911-4917.
- [5] S. Cheng, H. Liu, B.E. Logan, Electrochemistry Communications, 8 (2006) 489-494.
- [6] S.C. Popat, D. Ki, B.E. Rittmann, C.I. Torres, ChemSusChem, 5 (2012) 1071-1079.
- [7] C. Santoro, A. Agrios, U. Pasaogullari, B. Li, International Journal of Hydrogen Energy, 36 (2011) 13096-13104.
- [8] G.-C. Gil, I.-S. Chang, B.H. Kim, M. Kim, J.-K. Jang, H.S. Park, H.J. Kim, Biosensors and Bioelectronics, 18 (2003) 327-334.
- [9] Z. He, L.T. Angenent, Electroanalysis, 18 (2006) 2009-2015.
- [10] S. Ou, H. Kashima, D.S. Aaron, J.M. Regan, M.M. Mench, Journal of Power Sources, 314 (2016) 49-57.
- [11] S. Ou, PhD Dissertation in: Mechanical Engineering, University of Tennessee, Knoxville, TN, 2015, pp. 169
- [12] A.P. Borole, G. Reguera, B. Ringeisen, Z.-W. Wang, Y. Feng, B.H. Kim, Energy & Environmental Science, 4 (2011) 4813-4834.
- [13] Y. Feng, Q. Yang, X. Wang, B.E. Logan, Journal of Power Sources, 195 (2010) 1841-1844.
- [14] F. Zhang, M.D. Merrill, J.C. Tokash, T. Saito, S. Cheng, M.A. Hickner, B.E. Logan, Journal of Power Sources, 196 (2011) 1097-1102.
- [15] L. Ren, J.C. Tokash, J.M. Regan, B.E. Logan, international journal of hydrogen energy, 37 (2012) 16943-16950.
- [16] Y. Zhao, Master Thesis in: Environmental Engineering, The Pennsylvania State University, State College, PA, 2013, pp. 46.
- [17] A. Kato Marcus, C.I. Torres, B.E. Rittmann, Biotechnology and bioengineering, 98 (2007) 1171-1182.
- [18] M.M. Mench, Fuel cell engines, John Wiley & Sons, 2008.

- [19] S. You, Q. Zhao, J. Zhang, J. Jiang, C. Wan, M. Du, S. Zhao, Journal of Power Sources, 173 (2007) 172-177.
- [20] N.S. Malvankar, M. Vargas, K.P. Nevin, A.E. Franks, C. Leang, B.-C. Kim, K. Inoue, T.
- Mester, S.F. Covalla, J.P. Johnson, nature nanotechnology, 6 (2011) 573-579.
- [21] Z. Ren, H. Yan, W. Wang, M. Mench, J. Regan, Environ. Sci. Technol., 45 (2011) 2435.
- [22] P. Pacheco, An introduction to parallel programming, Elsevier, 2011.
- [23] C. Picioreanu, M.C. Van Loosdrecht, J.J. Heijnen, Biotechnology and bioengineering, 69 (2000) 504-515.
- [24] C. Picioreanu, J.-U. Kreft, M.C. van Loosdrecht, Applied and environmental microbiology, 70 (2004) 3024-3040.
- [25] P.C. Lichtner, Geochimica et Cosmochimica Acta, 49 (1985) 779-800.
- [26] B.E. Rittmann, A. Schwarz, H. Eberl, E. Morgenroth, J. Perez, M. Van Loosdrecht, O. Wanner, Water Science & Technology, 49 (2004) 163-168.
- [27] P.S. Stewart, Journal of bacteriology, 185 (2003) 1485-1491.
- [28] L. Yuan-Hui, S. Gregory, Geochimica et cosmochimica acta, 38 (1974) 703-714.
- [29] J.J. Beun, K. Dircks, M.C.M. Van Loosdrecht, J.J. Heijnen, Water Research, 36 (2002) 1167-1180.
- [30] R.B. Bird, W.E. Stewart, E.N. Lightfoot, Transport phenomena, John Wiley & Sons, 2007.
- [31] C. Multiphysics, in, COMSOL, AB, Burlington, Massachusetts, 2012.
- [32] T.C. Zhang, P.L. Bishop, Water Research, 28 (1994) 2267-2277.